RESEARCH PAPER

BJP | BRITISH PHARMACOLOGICAL SOCIETY

Molecular dynamics simulations of dihydro-β-erythroidine bound to the human α4β2 nicotinic acetylcholine receptor

Rilei Yu[1,2] | Han-Shen Tae[3] | Qingliang Xu[1,2] | David J. Craik[4] | David J. Adams[3] | Tao Jiang[1,2] | Quentin Kaas[4]

[1] Key Laboratory of Marine Drugs, Chinese Ministry of Education, School of Medicine and Pharmacy, Ocean University of China, Qingdao, China

[2] Laboratory for Marine Drugs and Bioproducts, Qingdao National Laboratory for Marine Science and Technology, Qingdao, China

[3] Illawarra Health and Medical Research Institute (IHMRI), University of Wollongong, Wollongong, NSW, Australia

[4] Institute for Molecular Bioscience, The University of Queensland, Brisbane, QLD, Australia

Correspondence
Rilei Yu, Key Laboratory of Marine Drugs, Chinese Ministry of Education, School of Medicine and Pharmacy, Ocean University of China, Qingdao 266003, China.
Email: ryu@ouc.edu.cn

Quentin Kaas, Institute for Molecular Bioscience, The University of Queensland, Brisbane, QLD 4072, Australia.
Email: q.kaas@imb.uq.edu.au

Background and Purpose: The heteromeric α4β2 nicotinic acetylcholine receptor (nAChR) is abundant in the human brain and is associated with a range of CNS disorders. This nAChR subtype has been recently crystallised in a conformation that was proposed to represent a desensitised state. Here, we investigated the conformational transition mechanism of this nAChR from a desensitised to a closed/resting state.

Experimental Approach: The competitive antagonist dihydro-β-erythroidine (DHβE) was modelled by replacement of the agonist nicotine in the α4β2 nAChR experimental structure. DHβE is used both in vitro and in vivo for its ability to block α4β2 nAChRs. This system was studied by three molecular dynamics simulations with a combined simulation time of 2.6 μs. Electrophysiological studies of mutated receptors were performed to validate the simulation results.

Key Results: The relative positions of the extracellular and transmembrane domains in the models are distinct from those of the desensitised state structure and are compatible with experimental structures of Cys-loop receptors captured in a closed/resting state.

Conclusions and Implications: Our model suggests that the side chains of α4 L257 (9′) and α4 L264 (16′) are the main constrictions in the transmembrane pore. The involvement of position 9′ in channel gating is well established, but position 16′ was only previously identified as a gate for the bacterial channels, ELIC and GLIC. L257 but not L264 was found to influence the slow component of desensitisation. The structure of the antagonist-bound state proposed here should be valuable for the development of therapeutic or insecticide compounds.

1 | INTRODUCTION

The Cys-loop receptors are the most diverse class of ionotropic neurotransmitter-gated ion channels and are also major contributors to the modulation of neuronal communication (Cecchini & Changeux, 2015; Nemecz, Prevost, Menny, & Corringer, 2016; Plested, 2016). Each of these receptors is activated by different neurotransmitters, and the most prevalent receptors in the brain are the **nicotinic ACh** (nAChR), **glycine**, **5-HT₃**, and **GABAₐ** receptors. They have a pseudo-symmetrical pentameric structure of homologous subunits and display an extracellular domain (ECD), a transmembrane domain (TMD), and a C-terminal domain. After a period of activation, Cys-loop receptors undergo desensitisation, which is an ensemble of non-conducting states characterised by a high affinity for agonists (Boyd & Cohen, 1980; daCosta & Baenziger, 2013; Quick & Lester, 2002). The receptors ultimately recover from desensitisation, adopting an agonist-sensitive resting state, which can be once again activated.

The nAChR is the prototypical member of the Cys-loop receptors because it was the first to be identified (Changeux, 2012). The pentameric organisation (Hucho & Changeux, 1973), agonist binding site location (Oswald & Changeux, 1982), and domain organisation and fold (Unwin, 2005) are shared features of Cys-loop receptors and were all discovered using nAChRs (Changeux, 2012). Despite the importance of nAChRs in the early characterisation of synaptic transmission, high-resolution structural biology studies focused on other members of the family until the recent study of the human α4β2 nAChR subtype in complex with **nicotine** by EM and X-ray crystallography (Morales-Perez, Noviello, & Hibbs, 2016; Walsh et al., 2018). As shown in Figure 1, the α4β2 nAChR ECD is a β-sandwich composed of 10 strands, denoted β1 to β10. The agonist binding sites are located at the interface between two subunits in the ECD contributed by a β-sheet of the complementary subunit and the A-, B-, and C-loops of the principal subunit. Each subunit contributes to the TMD by four sequential α-helices, M1–M4, with the M2 helices lining the central channel and interacting with the M1 and M3 helices.

The α4β2 nAChR, which is a pentamer of **nAChR α4 subunits** and **nAChR β2 subunits**, was crystallised in a non-conducting state, with the nicotine bound to the ECD and the TMD constricted at the intracellular exit (Morales-Perez et al., 2016). This structure was proposed to represent a desensitised state because of the decreased pore diameter in the intracellular side, similar to the GABAₐ and glycine receptor structures that were claimed representing the desensitised states (Du, Lü, Wu, Cheng, & Gouaux, 2015; Miller & Aricescu, 2014). It is also known that the α4β2 nAChR desensitises almost completely with steady-state application of a high concentration of nicotine.

Cys-loop desensitised conformations are highly similar to the open state except at the desensitised gate in the intracellular region of the TMD, whereas the resting state is structurally divergent from other activation states, displaying relative tilting and twisting of domains (Du et al., 2015). Therefore, the resting states of nAChRs are an essential missing element for describing nAChR activation states. Here, we used the crystal structure of the α4β2 nAChR to build a model of its complex with the competitive antagonist **dihydro-β-erythroidine** (DHβE), an *Erythrina* alkaloid, and investigate the conformational coupling from the ligand binding site in the ECD to the TMD by performing several molecular dynamics (MD) simulations. The resulting channel conformation displays the common features of Cys-loop receptors in a closed/resting state.

What is already known
- The X-ray and EM structures of the α4β2 nicotinic ACh receptor (nAChR) in a desensitised state were determined.

What this study adds
- The three-dimensional structure of the α4β2 nAChR bound to an inhibitor was proposed.
- Residues involved in pore gating of nAChRs were identified.

What is the clinical significance
- The structure of nAChRs in a closed state enables the design of nAChR inhibitors.
- Specific inhibitors of nAChR subtypes could be used to treat addiction and pain.

2 | METHODS

2.1 | Initial model of DHβE binding mode

An initial model displaying an interaction between DHβE and the orthosteric binding site of α4β2 nAChR was generated using the crystal structures of the complex between ACh binding protein (AChBP) and DHβE (PDB identifier 4alx; Shahsavar et al., 2012) and of human α4β2 nAChR in a desensitised state and bound by two nicotine molecules (PDB identifier 5kxi; Morales-Perez et al., 2016). Nicotine molecules were replaced by DHβE in the α4β2 nAChR structure by transferring their coordinates after structural superimposition of AChBP and nAChR ECD. Limited steric clashes were observed between the C-loops and DHβE molecules, and they were resolved by minimisation using AMBER 16 (AMBER, RRID:SCR_014230; Case et al., 2005).

2.2 | MD simulations

MD simulations of the α4β2 nAChR were performed using AMBER 16 (Case et al., 2005). The α4β2 nAChR bound with DHβE was inserted in a bilayer containing a 2:2:1 mixture of POPC (1-palmitoyl-2-oleoyl-sn-glycero-3-phosphocholine):POPE (1-palmitoyl-2-oleoyl-sn-glycero-3-phosphoethanolamine):cholesterol, similar to Grossfield, Pitman, Feller, Soubias, and Gawrisch (2008), with dimension of 100 × 101 × 105 Å, and the system solvated with TIP3P water molecules and Na⁺ and Cl⁻ ions such that the system was neutral with an overall concentration
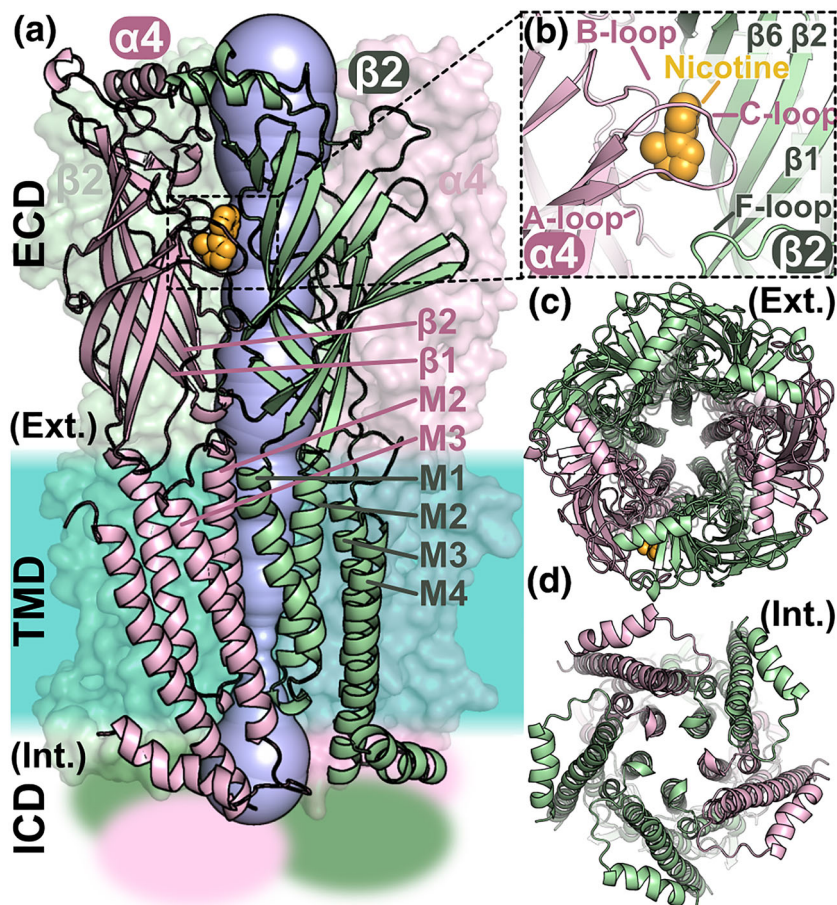
FIGURE 1 Structure of the heteropentameric ligand-gated ion channel α4β2 nAChR. (a) Domain and subunit organisation of the α4β2 nAChR and visualisation of the pore. The α4 and β2 subunits are coloured pink and green, respectively. The α4 and β2 subunits on the front shown are in cartoon representation and the other three subunits in surface representation. The nAChR is composed of three domains: an extracellular domain (ECD), a transmembrane domain (TMD), and an intracellular domain (ICD), the structure of which is unknown and is represented as fuzzy areas. The crystal structure of the α4β2 nAChR (PDB identifier 5kxi) was used to draw this figure. A nicotine molecule, coloured in orange, is bound in the orthosteric binding pocket. The pore of the channel is shown in blue, and the approximate location of the membrane region is shown as a turquoise area. (b) Orthosteric binding site occupied by a nicotine molecule. The A-, B-, and C-loops of the α4 subunits are labelled as is the F-loop and several β-strands from the β4 subunit. (c) View through the ECD of the central pore from the extracellular (Ext.) side. (d) View through the TMD of the central pore from the intracellular (Int.) side. The M2 helices of the TMD are lining the pore of the channel

of 0.15 M in CHARMM-GUI (http://www.charmm-gui.org; Lee et al., 2016). The temperature of the system was gradually increased to 310 K and was equilibrated for 500 ps in NVT and NPT ensembles, respectively, with the protein and lipids restrained with 10-kcal·mol^{-1}·Å^{-2} force. Langevin thermostat was used for the initial heating. For the second heating phase, an anisotropic Berendsen weak-coupling barostat was used to also equilibrate the pressure in addition to the use of the Langevin thermostat to equilibrate the temperature. Then the position restraints on the membrane were withdrawn, and the system was simulated for 20 ns in NPT. The position restraints on the protein were then gradually withdrawn in 10 steps of 5-ns MD simulations. Afterwards, unrestrained production run was performed. In the production run, the temperature was controlled using the Langevin thermostat, while the pressure was controlled using the anisotropic Berendsen barostat. Three production run simulations, referred here as Simulations 1, 2, and 3, were carried out for 700, 700, and 1,200 ns, respectively (Table S1). The three simulations were started from independently equilibrated systems. All simulations were performed using the Lipid14 force field (Dickson et al., 2014) for the lipids, AMBER14SB force field (Maier et al., 2015) for the protein, and the GAFF force field (Wang, Wolf, Caldwell, Kollman, & Case, 2004) for DHβE. The MD simulations used a time step of 2 fs, and all bonds involving hydrogen atoms were maintained to their standard length using the SHAKE algorithm (Ryckaert, Ciccotti, & Berendsen, 1977). Particle mesh Ewald (Darden, York, & Pedersen, 1993) was used

with a cut-off of 10 Å for non-bonded atoms interactions, and neighbour lists were updated every 10 steps. The Berendsen barostat is not ideal for simulations displaying large volume fluctuations (Shirts, 2013). However, this barostat was used because it was employed during the parametrisation of the lipid14 force field (Dickson et al., 2014) and because the volume of the system was stable during the production run simulations. After 400 ns, all three simulations reached equilibrium according to the backbone root-mean-square deviation from the starting conformation of the production run (Figure S1). Average values reported in the text were computed as the average values for the three simulations from 400 ns to the end of each simulation.

2.3 | Tilt angle calculations

The tilting angle of each subunit in the ECD was determined by measuring angles between the individual β-sheet core axes and the axis of the receptor in cylindrical coordinates. The Z axis was defined as the channel axis, and radial vectors r are perpendicular to the Z axis. The principal axis of each subunit in the ECD was obtained by three-dimensional least-square fitting of the Cartesian coordinates of the Cα atoms. The following definitions of the β-sheet core of each ECD subunit were used: residues 1–208 in the α4 subunit and residues 1–207 in the β2 subunit. The ECD radial tilt angle of each subunit in the ECD is the angle between the Z axis and the projected principal

axis of each subunit in the ECD onto the plane defined by the Z and r, which points from Z to the centre of the centre of mass (COM) of the subunit in the ECD. The ECD tangential tilt angle in the ECD is the angle between the Z axis and the projected principal axis of each subunit in the ECD onto the plane perpendicular to r. The M2 tilt angles were calculated using the same method as the ECD radial tilt angle. The M2 helix includes residues 240–262 for the α4 subunit and residues 239–261 for the β2 subunit.

2.4 | ECD–TMD twist angle calculations

The ECD–TMD twist angle measures the relative displacement of each subunit in the ECD and in the TMD, corresponding to an angle between two projected vectors in the normal to Z, that is, the radial plane. If the projection on the radial plane of the COM of the subunit contribution in the ECD and in the TMD are along the same radial vector, then the ECD–TMD twist angle of the subunit is null. In practice, the ECD–TMD twist angle was computed as the angle between two vectors projected in the radial plane: One vector is defined by the COMs of the entire receptor and of the subunit in the ECD, and the other vector is defined by the COMs of the entire receptor and the subunit in the TMD.

2.5 | Radius calculation

The radius of the pore along Z was calculated using the Hole 2.0 program (Smart, Neduvelil, Wang, Wallace, & Sansom, 1996) after aligning along Z the three-dimensional structures of the channel. The flow of water passing through the pore was computed using a python script (Python Programming Language, RRID:SCR_008394) implemented with the MDAnalysis package (Michaud-Agrawal, Denning, Woolf, & Beckstein, 2011).

2.6 | Electrophysiology

The [L257A] and [L264A] mutants of α4 subunit were generated using KAPA HiFi HotStart PCR kit (Roche, Basel, Switzerland) and confirmed by DNA sequencing (Macrogen, Seoul, South Korea). Plasmid constructs of human (h)α4 and hβ2 nAChR subunits were linearised for in vitro cRNA transcription using mMessage mMachine transcription kit (AMBION, Foster City, CA, USA). Stage V–VI oocytes (Dumont's classification; 1,200- to 1,300-μm diameter) were obtained from *Xenopus laevis*, defolliculated with 1.5-mg·ml⁻¹ collagenase Type II (Worthington Biochemical Corp., Lakewood, NJ, USA) at room temperature for 1–2 hr in OR-2 solution containing (in mM) 82.5 NaCl, 2 KCl, 1 MgCl$_2$, and 5 HEPES at pH 7.4. Oocytes were injected with 5-ng cRNA for human α4β2 (hα4β2) nAChR (concentration confirmed spectrophotometrically and by gel electrophoresis) using glass pipettes pulled from glass capillaries (3-000-203 GX, Drummond Scientific Co., Broomall, PA, USA). Oocytes were incubated at 18°C in sterile ND96 solution composed of (in mM) 96 NaCl, 2 KCl, 1 CaCl$_2$, 1 MgCl$_2$, and 5 HEPES at pH 7.4, supplemented with 5% FBS, 0.1-mg·L⁻¹ gentamicin

(GIBCO, Grand Island, NY, USA), and 100-U·ml⁻¹ penicillin–streptomycin (GIBCO). ND96 solution is the standard oocyte bathing solution used for electrophysiological recordings. Female *X. laevis* were sourced from Nasco (Fort Atkinson, WI, USA), and a maximum of three frogs were kept in purpose-built 15-L aquarium at 20–26°C with 12-hr light/dark cycle within the University of Sydney Laboratory Animal Services facility. Electrophysiological experiments were performed using oocytes obtained from three frogs ~5 years old. Frogs were anaesthetised with 1.7-mg·ml⁻¹ ethyl 3-aminobenzoate methanesulfonate (pH 7.4 with NaHCO$_3$), and for recovery, post-surgery animals were placed in fresh water at level below the nostrils. Frogs were left to recover for a minimum of 4 months between surgeries. Terminal anaesthesia with 5.0-mg·ml⁻¹ ethyl 3-aminobenzoate methanesulfonate (pH 7.4 with NaHCO$_3$) was performed on frogs at the sixth surgery. All procedures were approved by the University of Sydney and University of Wollongong Animal Ethics Committees.

Electrophysiological recordings were carried out 2–5 days post-cRNA microinjection. Two-electrode voltage clamp recordings of *X. laevis* oocytes expressing human nAChRs were performed at room temperature (21–24°C) using a GeneClamp 500B amplifier and pClamp9 software interface (Molecular Devices, Sunnyvale, CA, USA) at a holding potential −80 mV. Voltage-recording and current-injecting electrodes were pulled from GC150T-7.5 borosilicate glass (Harvard Apparatus, Holliston, MA, USA) and filled with 3-M KCl, giving resistances of 0.3–1 MΩ. Oocytes were perfused with ND96 solution using a continuous Legato 270 push/pull syringe pump perfusion system (KD Scientific, Holliston, MA, USA) at a rate of 2 ml·min⁻¹.

Initially, oocytes were briefly washed with ND96 solution followed by three applications of half-maximally effective concentration (EC$_{50}$) of nicotine for hα4β2 nAChRs. Washout with bath solution for 3 min was carried out between nicotine applications. Oocytes were incubated with DHβE for 5 min with the perfusion system turned off, followed by co-application of nicotine and DHβE with flowing bath solution. All solutions were prepared in ND96 + 0.1% BSA.

2.7 | Data and statistical analysis

The data and statistical analysis in this study comply with the recommendations of the *British Journal of Pharmacology* on experimental design and analysis in pharmacology. Peak current amplitudes before (nicotine alone) and after (nicotine + DHβE) DHβE incubation were measured using Clampfit version 10.7.0.3 software (Molecular Devices), where the ratio of nicotine + DHβE-evoked current amplitude to nicotine alone-evoked current amplitude was used to assess the activity of DHβE at hα4β2 nAChRs. Fast and slow decay time constants were obtained from exponential fit function. All electrophysiological data were pooled (n = 5–7) and are shown as means ±SEM. Data analysis was performed using GraphPad Prism 5 (GraphPad Prism, RRID:SCR_002798; GraphPad Software, La Jolla, CA, USA). The IC$_{50}$ was determined from concentration–response relationships fitted to a non-linear regression function and reported with error of

the fit. Data sets were compared using unpaired Student's *t* test. Differences were regarded statistically significant when *P* < .05.

2.8 | Materials

(−)-Nicotine hydrogen tartrate salt was from SIGMA (St. Louis, MO, USA) and DHβE hydrobromide from TOCRIS (Bristol, UK).

2.9 | Nomenclature of targets and ligands

Key protein targets and ligands in this article are hyperlinked to corresponding entries in http://www.guidetopharmacology.org, the common portal for data from the IUPHAR/BPS Guide to PHARMA-COLOGY (Harding et al., 2018), and are permanently archived in the Concise Guide to PHARMACOLOGY 2017/18 (Alexander et al., 2017).

3 | RESULTS

3.1 | DHβE binding mode and interactions

At the end of the three simulations, the orientation of DHβE molecules in the two binding sites of α4β2 nAChR was similar to that of the crystal structure of the complex between DHβE and the *Lymnaea stagnalis* AChBP (Shahsavar et al., 2012; Figure 2a–c). The MolProbity scores (Williams et al., 2018) of the final frame of each simulations were between 1.03 and 1.13, corresponding to the 100th percentile, suggesting that the geometry of the generated models is excellent. During the MD simulations, DHβE was located approximately at the centre of the orthosteric binding site, which comprises W156, Y197, and Y204 of the principal subunit and N109 and L121 of the complementary subunit. The positively charged nitrogen atom of DHβE formed a stable hydrogen bond with the backbone carbonyl oxygen of W156, and it occupied a position compatible with a cation–π interaction with the aromatic ring of the same residue (Figure 2d,e). Similar interactions between DHβE and the receptor were displayed by W143 in the binding site of AChBP (Shahsavar et al., 2012).

A water molecule entered each binding site during the simulations and created three hydrogen bonds between the oxygen atom of the DHβE methoxy group and the carboxyl and nitrogen atoms of N109 and L121, respectively. A similar water molecule is present in the crystal structure of DHβE in complex with AChBP (Shahsavar et al., 2012). In one binding site during Simulation 1, the water molecule was exchanged by another that established a similar hydrogen bond network and remained stable until the end of the simulation (Figure 2e).
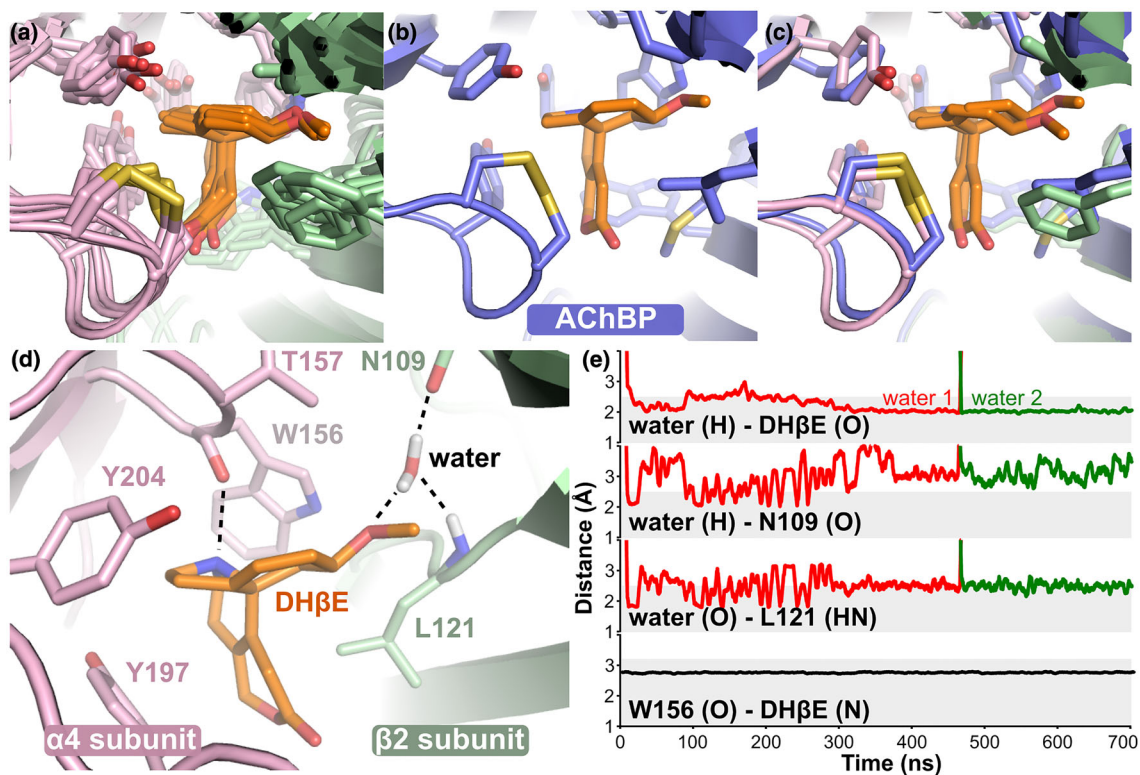
FIGURE 2 Binding mode of DHβE in the orthosteric binding site of α4β2 nAChR. (a) Comparison of the binding modes of DHβE at the end of the three simulations and for the two binding sites of α4β2 nAChR (in total six structures). (b) Binding mode of DHβE in the binding site of AChBP (PDB identifier 4alx). (c) Overlay of the binding mode of DHβE in the AChBP binding site (blue) and in the α4β2 nAChR binding site (pink and green) at the end of Simulation 1. (d) Details of molecular interactions of DHβE with the receptor in one of the two α4(+)β2(−) binding sites in Simulation 1 at 700 ns. (e) Evolution of distances between the water molecules represented in panel (a) and DHβE as well as between the backbone oxygen of W156 and DHβE during Simulation 1. The grey area represents the distance considered as relevant to the formation of a hydrogen bond

In other binding sites and simulations, the bridging water molecule was stable during the entire simulation (not shown).

3.2 | Conformation of the C-loop

The opening of the C-loop of the α4 subunit bound with DHβE was approximately 4 Å larger during the MD simulations than in the crystal structure of α4β2 nAChR bound with nicotine, which is compatible with an interaction with antagonists (Figure 3a,b and Table S2). The C-loop opening of approximately 13 Å in our model of the α4β2/DHβE is similar to the binding of antagonists in crystal structure of AChBP (Figure 3c). In particular, the crystal structure of the complex between AChBP and DHβE displayed an opening distance of the C-loop similar to our model of the α4β2 nAChR/DHβE (Shahsavar et al., 2012).

3.3 | Relative domain tilting and twisting

Figure 4 shows the evolution of the tilting and twisting angles during the MD simulations of α4β2 nAChR in complex with DHβE compared to the crystal structure of α4β2 nAChR/nicotine. The average ECD radial tilt angle measured during the MD simulations of the DHβE-bound α4β2 nAChR was of 4.6° (Figure 4a). By contrast, the nicotine-bound nAChR crystal structure displayed an ECD radial tilt angle of only 0.4° (Table S4). The ECD tangential tilt of the DHβE-bound α4β2 nAChR was of 11.1°, which is similar to the 10.3° measured in the nicotine-bound structure. The relative rotation of the ECD and of the TMD (ECD–TMD twist angle) initially changed

by ~3° compared to the nicotine-bound structure but became similar over time for Simulations 1 and 3 (Figure 4c). By contrast, Simulation 2 did not display a "recovery" of the ECD–TMD twist angle until the end of the simulation. The time traces corresponding to each subunit are not synchronous (Figure S2), which was observed in earlier molecular simulations of Cys-loop receptors (Calimet et al., 2013; Liu et al., 2008).
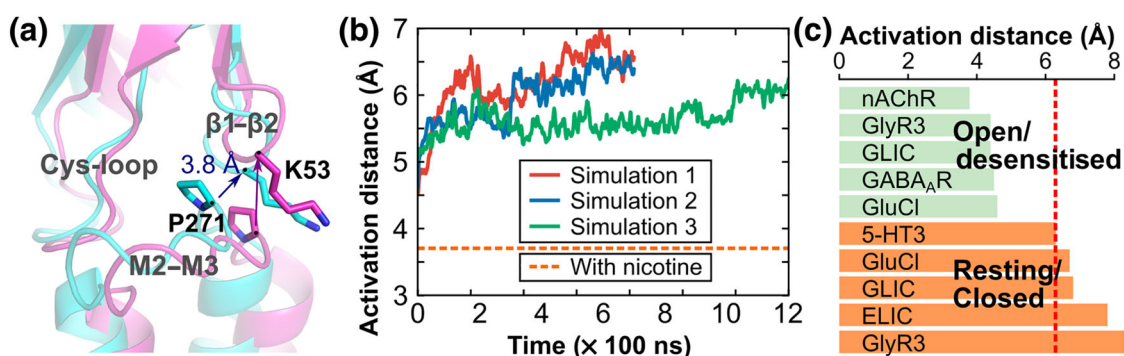
3.4 | Interface between the ECD and TMD

As illustrated in Figure 5a, the interface between the ECD and TMD comprises a linker between the ECD β10 strand and the M1 α-helix of the TMD, as well as three loops named β1–β2 linker, M2–M3 linker, and the Cys-loop. A strong energy coupling was observed between the central part of the M2–M3 linker and the β1–β2 linker (P271; Gupta, Chakraborty, Vij, & Auerbach, 2017), and we used the distance between the central residues of these linkers, which we call the "activation distance," to characterise different activation states (Table S2). The experimental structures of the glycine receptor, GLIC, and GluCl captured in various activation states provide evidence that the closed/resting state displays an activation distance that is longer than that of the open or desensitised states (6–8 Å compared to 4–5 Å). Accordingly, the crystal structure of α4β2 nAChR in a desensitised state has an ECD–TMD linker distance of 3.7 Å. The activation distance measured during the MD simulations of the DHβE-bound α4β2 nAChR was 5.5–6.5 Å, falling in the distance range of the resting/closed states (Figure 5b,c).
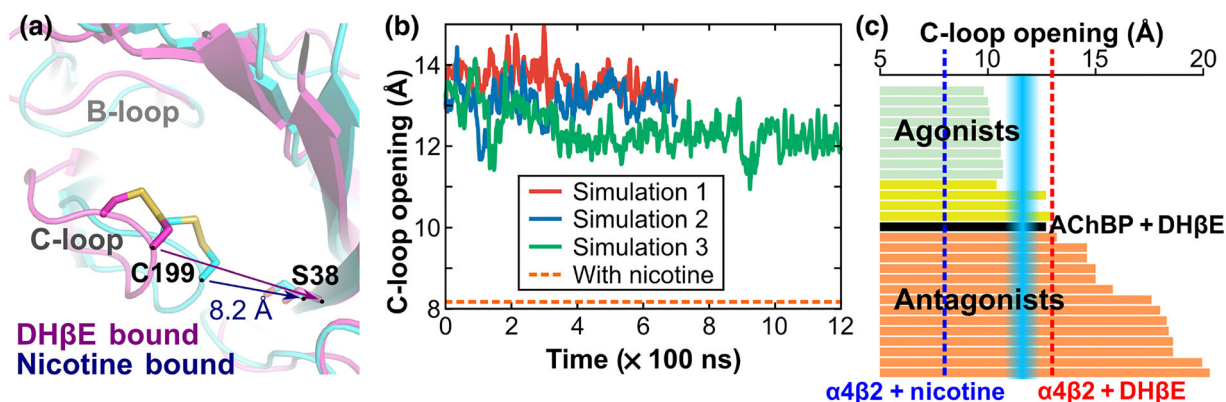
FIGURE 3 Conformation of C-loop of the α4β2 nAChR in complex with DHβE and comparison with ACh binding proteins (AChBPs) in complex with agonists and antagonists. (a) Superimposition of a molecular model of the complex between α4β2 nAChR and DHβE (magenta) and of the X-ray crystallographic structure of the human α4β2 nicotinic receptor interacting with nicotine (blue). The distance used to characterise the C-loop opening in the α4β2 nAChR was measured between the Cα of Cys199 of the α4 subunit and the Cα of Ser38 of the β2 subunit. (b) Distance characteristic of the C-loop "opening" (averaged between the two binding sites) during the three MD simulations of α4β2 nAChR/DHβE complex. The orange dashed line represents the C-loop opening in the nicotine/α4β2 nAChR complex (PDB identifier 5kxi). (c) C-loop opening distance in crystal structures of AChBP in complex with agonists (green), antagonists (orange), or compounds with dual activity (yellow). The blue zone represents the approximate boundary between agonists and antagonists. The red dashed line shows the average C-loop distance measured during the MD simulations of the α4β2 nAChR/DHβE system. The blue dashed lines represent the C-loop opening distance in the crystal structure of the α4β2 nAChR/nicotine complex. The AChBP structures that were analysed in panel (c) are listed in Table S3. The evolution of the C-loop opening distance of each binding site for the three simulations is shown in Figure S2
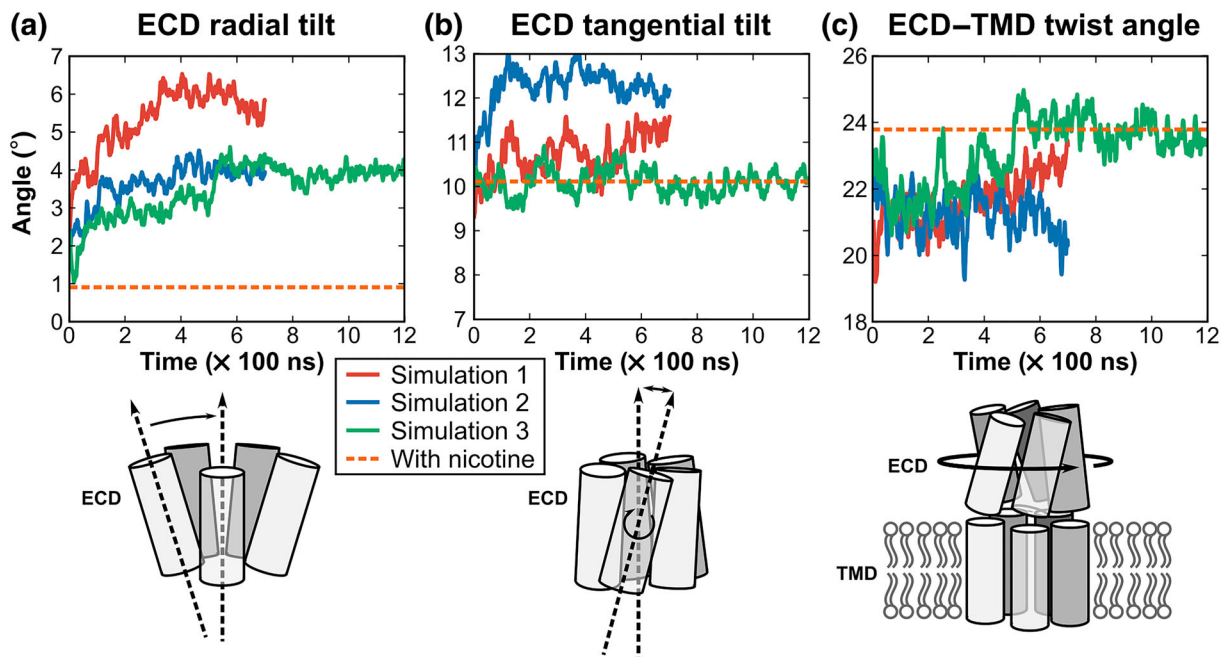
FIGURE 4 Domain tilting and twisting during the simulations of α4β2 nAChR bound with DHβE. (a) Radial tilt angle of the ECDs of the α4β2 nAChR in complex with DHβE. (b) Tangential tilt angle of the ECDs of the α4β2 nAChR in complex with DHβE. (c) Twist angles between the ECD and TMD of the α4β2 nAChR bound with DHβE. Data for Simulations 1, 2, and 3 are represented as red, blue, and green curves, respectively. The data represented here are the average of measurements made for the five subunits, and measurements for individual subunits are shown in Figure S2. The orange dashed line represents the measurement made in the nicotine/α4β2 nAChR complex (PDB identifier 5kxi)


FIGURE 5 Interface between the ECD and TMD of the α4β2 nAChR bound with DHβE. (a) Overlay between the final frame of the Simulation 1 (i.e., α4β2 nAChR bound with DHβE; magenta) and the crystal structure of the α4β2 nAChR bound with nicotine (cyan). (b) Activation distance measured during the MD simulations of the DHβE/α4β2 nAChR system. The activation distance was defined in the α4 subunit as the distance between the Cα atoms of K53 (centre of the β1–β2 linker) and P271 (centre of the M2–M3 linker). In the β2 subunit, the activation distance is measured between the Cα atoms of R48 (β1–β2 linker) and P263 (M2–M3 linker). The orange dashed line indicates the distance in the experimental structure of α4β2 nAChR bound with nicotine (PDB identifier 5kxi). (c) Activation distance measured in experimental structures of several Cys-loop receptors in either the open/desensitised or resting/closed states. The red dashed line represents the average activation distance measured in the three simulations. Panel (b) shows the average measurement between the five subunits, and the measurements made for each subunit are shown in Figure S2

3.5 | Tilt of the pore-lining α-helix M2

As shown in Figure 6, the M2 of the DHβE-bound receptor is approximately parallel with the central axis, with an average radial tilt of only 2.9°, whereas the average radial tilt angle in the crystal structure of the α4β2 nAChR in a desensitised state is 8.4°. The average M2 tilt angle of Simulation 3 is 4.3°, which is higher than that of the other

two simulations. This difference originates from a β2 subunit that did not change its tilt orientation over the course of the simulation (Figure S2). Overall, the ECD of the α4β2 nAChR bound with DHβE was tilted outward relative to the crystal structure of the α4β2 nAChR in a desensitised state (Morales-Perez et al., 2016; Figure 4b), and the upper segment of M2 was measured to have tilted inward compared to the same experimental structure (Figure 6b). An analysis of most
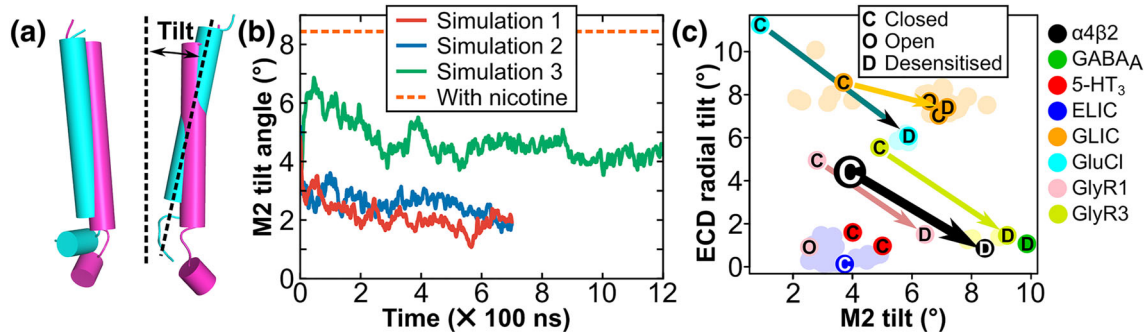
FIGURE 6 Comparison of the M2 tilt angle of each subunit of α4β2 nAChR bound with DHβE and analysis of the tilt angles of Cys-loop receptors. (a) Overlay of the M2 α-helix structures in the last frame (700 ns) of MD Simulation 1 of DHβE (magenta) with the crystal structure of the α4β2 nAChR in a desensitised state (cyan). (b) Average M2 tilt angle measured during α4β2/DHβE MD simulations. The orange dashed line indicates the M2 tilt angle in the experimental structure of α4β2 nAChR bound with nicotine (PDB identifier 5kxi). The measurements made for each subunit are in Figure S2. (c) Comparison of the ECD radial tilt and M2 tilt angles for all Cys-loop receptors experimental structure as well as with the last frame of Simulation 3, which is indicated by a larger black circle labelled with a white C letter. The activation state of a number of experimental structures has been proposed and labelled with a letter: C (closed/resting), O (open), or D (desensitised). The unlabelled data points have been faded for clarity. Arrows have been drawn from the closed/resting conformation to the desensitised conformation for each Cys-loop receptor. The experimental structures as well as their corresponding tilt angle values are listed in Table S3

available experimental structures of Cys-loop receptors, shown in Figure 6c, suggests that this coupled movement of ECD and M2 between the closed/resting and desensitised states is a general feature of Cys-loop receptors.

3.6 | Characterisation of the pore in the TMD

As shown in Figure 7a,b, the pore of the channel in the DHβE-bound simulations dried out between L257 (9′) and L264 (16′) (see Figure S3 for M2 numbering), whereas water molecules were abundant in this section of the pore at the beginning of the simulation. The upper region of the pore, that is surrounding position L264, is more constricted in the DHβE simulations than in the crystal structure of

the desensitised state structure (Morales-Perez et al., 2016; Figure 7 c,d). The lower region of the pore displayed a similar trend but to a lesser extent (Figure 7d), suggesting that the pore transited from a desensitised state to a closed/resting state by closure of the upper region of the pore. In addition to a translation towards the centre of the pore, the M2 helices also rotated along their axis, resulting in a different orientation of the L257 and L264 side chains (Figure 7c). The 9′ position of the TMD was also identified as a gate in the closed/resting state in the experimental structures of several other ligand-gated ion channels from a range of sources. These are the bacterial receptors from *Gloeobacter violaceus* (GLIC), from *Erwinia chrysanthemi* (ELIC); the invertebrate glutamate-gated chloride channel (GluCl) and the mammalian homomeric **α1 glycine** receptor (GlyR1) the homomeric
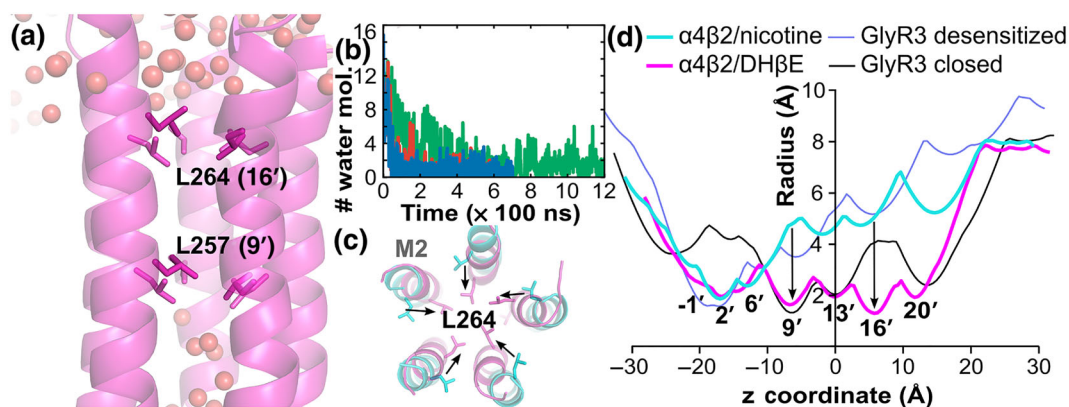
FIGURE 7 Pore in the TMD of the α4β2 nAChR when in complex with DHβE. (a) Distribution of water molecules (spheres) in the TMD channel of the α4β2 nAChR bound with DHβE in the final frame of one of the simulations. (b) Number of water molecules passing the gate L257 over the time of the three simulations. Simulations 1, 2, and 3 are in red, blue, and green, respectively. (c) Overlay of the structures of the M2 helices forming the pore in the TMD in the final frame of Simulation 1 of the α4β2/DHβE complex (magenta) and of the crystal structure of the desensitised state (PDB identifier 5kxi, cyan) as viewed from the extracellular side of the membrane. (d) Comparison of the TMD channel radius profiles of the α4β2 nAChR and GlyR3 in the closed/resting and desensitised states. The radius profiles were computed using Hole. Residues L257 (9′) and L264 (16′) create the main constrictions in the pore radius profiles, and these gate residues are shown in stick representation in panels (a) and (c)

α3 glycine receptor (GlyR3) and the 5-HT$_3$ receptor (Table S2). Additionally, the 9′ position is a hydrophobic residue in all human Cys-loop receptors (Figure S3), suggesting that the gating function of the 9′ position is conserved across the Cys-loop receptors. Similarly, the 16′ position is also responsible for gating the TMD in the crystal structures of the bacterial ELIC and GLIC receptors (Table S2, Figure S4), but it is not a site of constriction for the GlyR1, GlyR3, GluCl, and 5-HT$_3$ receptors (Figure 7d, Table S2), indicating that the function of this position as a gate is not conserved within the Cys-loop family.

3.7 | Functional importance of L257 (9′) and L264 (16′)

We experimentally probed the functional importance of α4 L257 (9′) or α4 L264 (16′) by mutating them individually into Ala and measuring activation and inhibition of the mutated receptors (Figure 8). The Ala substitutions increased the sensitivity for agonist nicotine by twofold,

but they had no impact on the inhibition by DHβE (Figure 8a,b). An increased sensitivity for agonist has been also reported for the α7 L9′V mutation of the homopentameric α7 nAChR (Revah et al., 1991), but we provide the first identification of nAChR position 16′ influencing agonist activity. The two mutated positions are distant from the ECD and therefore should not influence nicotine or the antagonist affinity, as confirmed by the benign substitutions for DHβE inhibition, but the agonist activity is influenced by the mutations. We propose that the mutations could destabilise the resting states, facilitating the transition from the resting states to open state or by stabilising the open state.

The nicotine (10 μM)-evoked current amplitude was increased more than 20-fold by each substitution (Figure 8c). A similar increased conductance was reported for 9′ mutants of the α7 nAChR (Revah et al., 1991); especially the mutation of Leu9′ into Val or small hydrophilic residues renders permeable one of the fast desensitised states, increasing the number of conducting states of the channel and
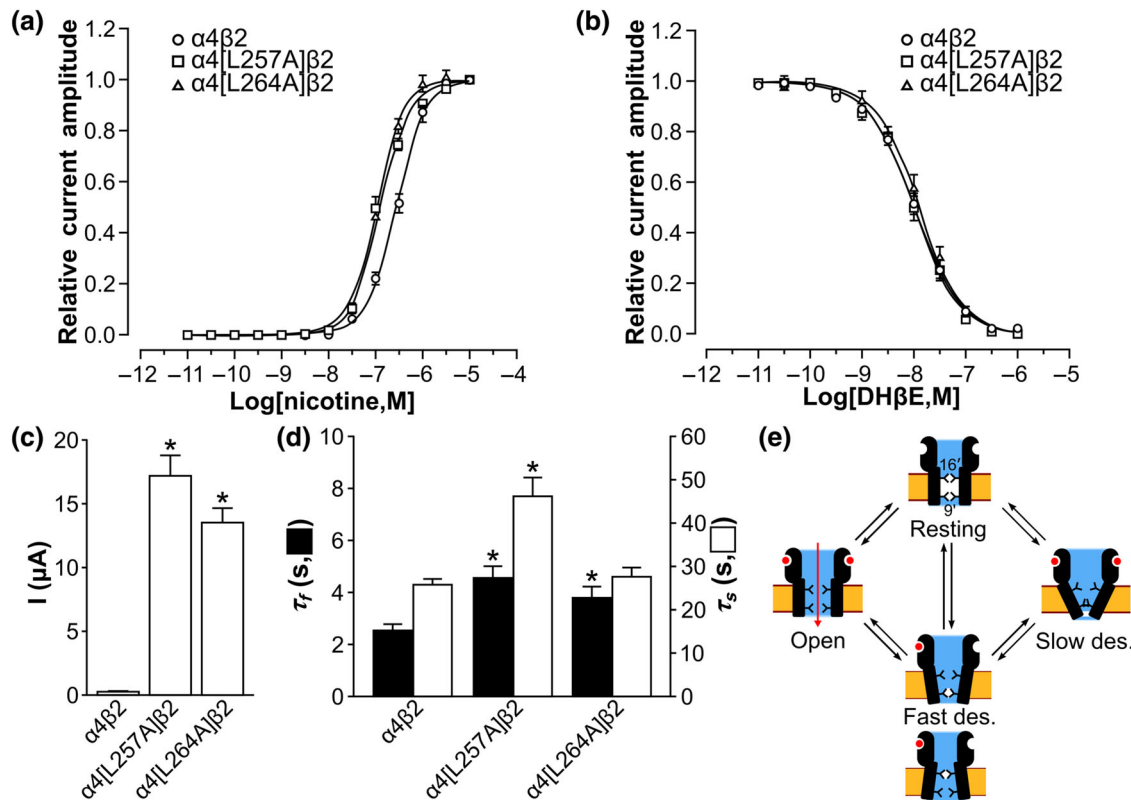
FIGURE 8 Electrophysiological characterisation of α4β2 nAChR mutated at positions α4 L257 or α4 L264. (a) Concentration–response relationship of relative nicotine-evoked current amplitude mediated by human α4β2 (hα4β2), hα4[L257A]β2, and hα4[L264A]β2 nAChRs. The EC$_{50}$ values of hα4β2, hα4[L257A]β2, and hα4[L264A]β2 nAChRs were of 276.7 ± 14.2 nM, 117.2 ± 4.7 nM, and 109.9 ± 3.2 nM (mean ± SEM, n = 5), respectively. (b) Concentration–response relationship of relative nicotine-evoked current amplitude mediated by hα4β2, hα4[L257A]β2, and hα4[L264A]β2 nAChRs in the presence of 10-pM to 1-μM dihydro-β-erythroidine (DHβE). The IC$_{50}$ values (mean ± error of the fit) of DHβE at hα4β2, hα4[L257A]β2, and hα4[L264A]β2 nAChRs were of 10.1 ± 0.6 nM, 9.7 ± 0.6 nM, and 12.6 ± 0.9 nM (n = 5–7 oocytes for each concentration), respectively. The variation in n was due to the viability of oocytes during experiments. (c) Nicotine (10 μM)-evoked current amplitude of hα4β2, hα4[L257A]β2, and hα4[L264A]β2 nAChRs. Data shown are means ± SEM, n = 5, *P < .05, significantly different from hα4β2; unpaired Student's t test.. (d) hα4β2, hα4[L257A]β2, and hα4[L264A]β2 nACh-mediated current decay time constant of the fast (τ$_f$) and slow (τ$_s$) components evoked by 10-μM nicotine. Data shown are means ± SEM; n = 5. *P < .05, significantly different from hα4β2; unpaired Student's t test. (e) Mechanistic model of hα4β2 nAChR activation states. The positions 9′ and 16′ in the TMD are represented as gates that could block the channel in the two independent fast desensitised states

therefore conductance (Bertrand et al., 1992; Revah et al., 1991). Position 9′ is therefore the only hydrophobic gate of at least one of the desensitised states of the α7 nAChR (Bertrand et al., 1992). For α4β2 nAChR, both the α4[L257A] (L9′A) and α4[L264A] (L16′A) mutants had increased whole-cell current amplitude, suggesting that they could be the unique hydrophobic gates of distinct fast desensitised states. We further observed that the ACh EC$_{50}$ of the wild-type α4β2 nAChR was 4 μM whereas the EC$_{50}$ of L264A mutant was 0.6 μM. A similar increase in the sensitivity of α7 nAChR after position 9′ mutation was reported and interpreted as stabilisation of a desensitised state by ACh that is only gated by position 9′ (Revah et al., 1991). The decrease in the ACh EC$_{50}$ of α4[L264A]β2 nAChR compared to the wild-type α4β2 therefore suggests the existence of a desensitised state that is only gated by position 16′. We nevertheless note that the stabilisation of the open state and an increased single channel conductance are alternative explanations to the increased current amplitude of the α4[L264A]β2 nAChR mutant.

Consistent with the fast desensitised states of the mutated channels becoming leaky, the current decay time constant of the fast desensitisation component (τ_f) was prolonged for both hα4[L257A]β2 and hα4[L264A]β2 compared to the wild type (Figure 8d). The α4β2 nAChR appears to behave similarly to the α7 nAChR upon mutation of the 9′ position (Bertrand et al., 1992; Revah et al., 1991), but the effect of DHβE on these two nAChRs differs. Indeed, DHβE was shown to activate the [L9′T]α7 nAChR by stabilising a fast desensitised state that became permeable with the α7 L9′T mutation (Bertrand et al., 1992). In contrast, we did not observe the potentiation of the receptor by DHβE for hα4[L257A]β2 and hα4[L264A]β2 (Figure 8b), indicating that DHβE stabilises a closed state that is not rendered permeable by the α4 L257A or the α4 L264A mutations, in agreement with our proposed molecular model where both positions act as gates.

The nicotine-evoked current decay time constant for the slow component (τ_s) of hα4[L264A]β2 (L16′A) was comparable to that of the wild type, whereas that of hα4[L257A]β2 (L9′A) was significantly prolonged (Figure 8d). We propose two hypotheses to interpret this result; first is that L257 (9′) is important for stabilising or gating the slow desensitised state but not L264 (16′), and second, the slow desensitised state can only be reached from the fast desensitised states that are destabilised by L257A (9′) substitution, but not by L264A (16′). The crystal structure and EM structures of the hα4β2 nAChR have been proposed to represent a desensitised state, which is probably a slow desensitised state because the fast desensitised state is short-lived. The pore radius at position 9′ in these structures is approximately 3.5–4.5 Å (Table S2), which would not prevent conduction, suggesting that position 9′ is not a gate of the slow desensitised state, potentially invalidating our first hypothesis. Nevertheless, most experimental structures of eukaryote Cys-loop receptors that were described as the desensitised state display a TMD pore that is more open in the extracellular side than in the intracellular side (Table S2; Plested, 2016). Consistent with this model of a slow desensitised state, the L257 (9′) is closer to the intracellular side than L264 (16′).

4 | DISCUSSION

We determined the binding mode of the competitive antagonist DHβE at the α4β2 nAChR using three MD simulations covering a total of 2.6-μs simulation time. The orientation of DHβE molecules in the two binding sites of α4β2 nAChR was similar to that of the crystal structure of the complex between DHβE and the *L. stagnalis* AChBP (Shahsavar et al., 2012). Invertebrate AChBPs are structural surrogates of the ECD of nAChRs and have been extensively used due to their comparatively easier recombinant expression and ability to be crystallised in complex with various nAChR ligands (Bouzat et al., 2004; Brejc et al., 2001; Shahsavar, Gajhede, Kastrup, & Balle, 2016). Interestingly, a water molecule entered each binding site during the simulations and created hydrogen bonds between the DHβE and two residues from the complementary subunit. Similar water-mediated hydrogen bonds were observed in the five binding sites of the crystal structure of AChBP bound with DHβE (Shahsavar et al., 2012). The striking similarity of molecular interactions in the orthosteric binding sites between DHβE and AChBP or α4β2 nAChR provides strong support to the practice of using AChBP as a structural surrogate of nAChRs (Shahsavar et al., 2016).

A proposed paradigm of antagonism compared to agonism of nAChRs is that agonists stabilise the C-loop into a relatively closed conformation whereas antagonist binding results in a larger opening of the C-loop (Tabassum, Ma, Wu, Jiang, & Yu, 2017). In our simulations, the C-loop of the α4β2 nAChR/DHβE displayed an open conformation similar to that of the crystal structure of the complex between AChBP and DHβE (Shahsavar et al., 2012). The C-loop conformation correlates with the agonist or antagonist activity of the ligand, but the C-loop itself is not essential for gating as it could be replaced by a poly-glycine linker (Purohit & Auerbach, 2013).

A comparison of Cys-loop receptor structures reveals that the activation states are characterised by different relative orientations of domains within each subunit (Nemecz et al., 2016). These orientations are described in terms of relative tilting (also called "blooming") between the ECD and TMD domains of each subunit and the twisting between the ECD and the TMD (Cecchini & Changeux, 2015; Gupta et al., 2017; Nemecz et al., 2016). During the MD simulations of the DHβE-bound α4β2 nAChR from the initial nicotine-bound nAChR crystal structure, the ECD as a whole experienced a 2.6° rotation relatively to the TMD.

Over the course of the MD simulations, the structure of the interface between the ECD and TMD of the α4β2 became similar to that of experimental structures of Cys-loop receptors in a closed/resting state. The β1–β2 and M2–M3 linkers are crucial for Cys-loop activity (Bouzat, 2012) and undergo conformational changes in different activation states of several Cys-loop receptors (Nemecz et al., 2016). The activation distance measured during the MD simulations of the DHβE-bound α4β2 nAChR was 6.0–6.5 Å, suggesting that the receptor adopts a closed/resting state during the MD simulations. The interaction between the α7 nAChR embedded in a pure POPC membrane and a large competitive inhibitor peptide, **α-conotoxin ImI**, was recently studied using MD simulations (Chiodo, Malliavin, Giuffrida,

Maragliano, & Cottone, 2018). The activation distance of this system was reported to be 12 Å, which is substantially larger than in our study and compared to other Cys-loop receptor structures.

The coupled movement of ECD and M2 between the closed/resting and desensitised states is a general feature of Cys-loop receptors. A similar opposite change of direction of ECD and TMD between the desensitised or open states versus the closed/resting state was also suggested from MD simulations starting from the crystal structure of GluCl and of the low-resolution EM structure of the muscle-type nAChR (Calimet et al., 2013; Liu et al., 2008). The closed/resting states of Cys-loop receptors appear to have, in general, an M2 tilt angle below 5°, whereas the desensitised states have larger values. The pore of the channel in the TMD is lined by the M2 helices, and the change of orientation of these helices consequently affects the volume of the pore.

The combination of rotation and translation of the M2 helices contributed to changing the shape of the pore, and the residues responsible for the major constrictions are E247 ($-1'$), L257 ($9'$), and L264 ($16'$). The five E247 residues, one from each subunit, form a ring of negatively charged residues that selectively filters cations (Bouzat, 2012). We propose that L257 and L264 are the hydrophobic gates responsible for the closing/opening of the channel to the passage of water and ions. A previous MD study of the low-resolution EM structure of the *Torpedo marmorata* muscle-type nAChR suggested that the hydrophobic gates were at positions $9'$ and $13'$ (Liu et al., 2008), contrasting with our identification of positions $9'$ and $16'$. The TMD of the neuronal and muscle-type nAChRs shares a high-sequence identity, and we propose that either the EM structure used as a starting point of the simulation did not have high enough resolution or that the computational time used for this simulation was too short to observe

a complete transition to the closed/resting state (30 vs. 700 to 1,200 ns in our simulations).

We experimentally probed the functional importance of L257 ($9'$) and L264 ($16'$) by mutating them individually into Ala and measuring activation and inhibition of the mutated receptors. Overall, the α4 L257A mutation caused a larger current amplitude and prolonged decay time constant for both the fast and slow components of desensitisation. The L257 ($9'$) is located in the middle of the TMD and is conserved across Cys-loop receptor families (Figure S3). The crystal structures of GlyR1, GlyR3, GluCl, GLIC, 5-HT$_3$, and ELIC in a closed/resting state support the hypothesis that the $9'$ position forms a hydrophobic gate (Table S2). The $16'$ position is located in the upper segment of the M2, which is less conserved than L257 (Figure S3). This position is a hydrophobic gate for two bacterial channels, GLIC and ELIC, in a closed/resting state (Figure S4) but not for the eukaryotic Cys-loop receptors GlyR1, GlyR3, GluCl, GABA$_A$ and 5-HT$_3$ (Table S2). Our mutagenesis studies suggest that L264 ($16'$) affects the current amplitude (cation influx) and acts as a hydrophobic gate for the α4β2 nAChR, controlling the transition between the resting, open, and some fast desensitised states but not to the slow desensitised states.

In summary, MD simulations of α4β2 nAChR bound with DHβE suggested that the receptor underwent a sequence of structural events resulting in the closure of the ion pore in the TMD (Figure 9). Binding of DHβE resulted in a larger opening of the C-loop of the two α4 subunits. The introduction of DHβE in the binding pocket also resulted in an outward tilting of the ECD β-sheet core. The outward movement of the ECD was transmitted to the TMD through communication between the β1–β2 linker and the M2–M3 linker. The β1–β2 linker moved upward, which resulted in the inward
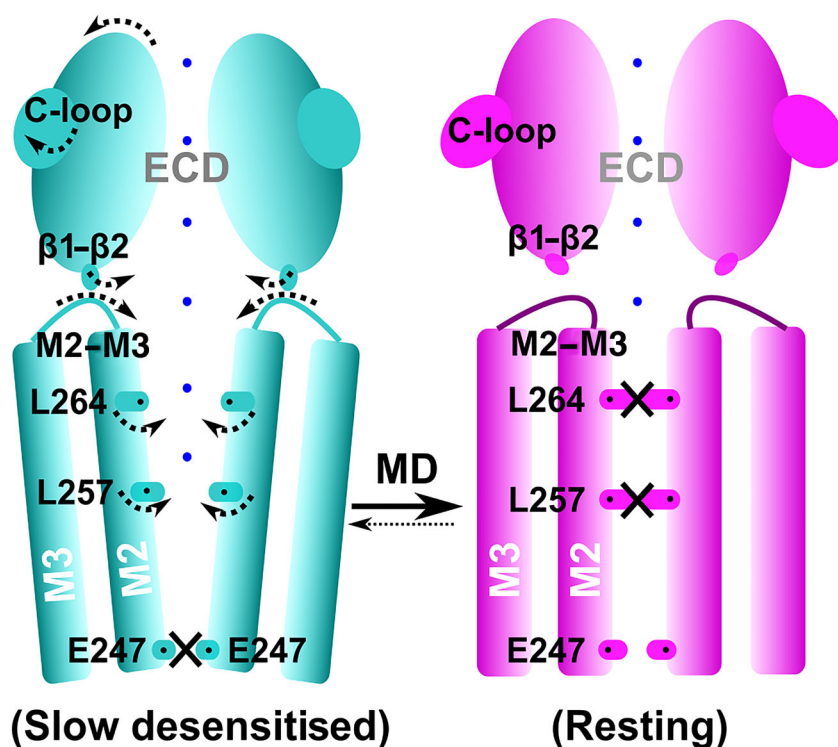
FIGURE 9 Schematic representation of the conformation changes occurring during the transition from a desensitised state to a closed/resting state for the α4β2 nAChR. Arrows indicate the motion of the ECD, M2, loops (C-loop, β1–β2 linker, and M2–M3 linker), and the side chains of the L264 and L257 residues. Constriction points in the channel are represented by black crosses. The parts of the channel available to cations are illustrated by blue dots

movement of the M2–M3 linker and the upper segment of the M2 helix. The translation and rotation movements of the M2 helix resulted in repositioning of the side chains of L257 and L264 in the centre of the pore, causing its closure (Figure 9). The structure of the antagonist-bound closed/resting state of α4β2 nAChR that we propose is globally similar to the experimental structures of other Cys-loop receptors in a closed/resting state, some being bound by antagonist molecules as well. Compared to the experimental structure of α4β2 nAChR in the desensitised state, the closed/resting state displays conformational differences in all parts of the receptor. The three simulations that we carried out led to similar, but not identical, changes of conformations of the receptor, and a longer simulation time would be required for better convergence, which will hopefully be possible with increased computational power. In consideration of the limited simulation time, the final MD relaxed model represents a closed state or a meta-stable conformation leading to the closed state.

The α4β2 nAChR is the most abundantly expressed subtype in the human brain, and it is linked to cognition and memory (Grupe, Grunnet, Bastlund, & Jensen, 2015). It is associated with a range of CNS disorders, including depression, attention deficit and hyperactivity disorders, cognitive impairments, and nicotine addiction (Dineley, Pandya, & Yakel, 2015; Grupe et al., 2015). For example, competitive antagonists targeting the resting state appear to be important for smoking cessation drugs for attenuating nicotine-induced reinforcement (Rollema & Hurst, 2018). Competitive nAChR antagonists are also insecticides, such as triflumezopyrim (DuPont), which is used to control rice grasshoppers (Crossthwaite et al., 2017). The structure that we propose should therefore be valuable for studying the activity of therapeutics or insecticidal compounds targeting the closed/resting state of vertebrate and insect nAChRs.

CONFLICT OF INTEREST

The authors declare no conflicts of interest.

AUTHOR CONTRIBUTIONS

R.Y. performed and supervised the experiments and wrote the manuscript. H.-S.T. performed the experiments and provided critical comments on the manuscript. Q.X. performed the experiments. D.J.C. provided critical comments on the manuscript. D.J.A. supervised the experiments and provided critical comments on the manuscript. T.J. supervised the experiments and provided critical comments on the manuscript. Q.K. developed the concept, performed the experiments, and wrote the manuscript.

DECLARATION OF TRANSPARENCY AND SCIENTIFIC RIGOUR

This Declaration acknowledges that this paper adheres to the principles for transparent reporting and scientific rigour of preclinical research as stated in the *BJP* guidelines for Design & Analysis, and Animal Experimentation, and as recommended by funding agencies, publishers, and other organisations engaged with supporting research.

ORCID

Rilei Yu https://orcid.org/0000-0001-6625-2014
Han-Shen Tae https://orcid.org/0000-0001-8961-7194
David J. Craik https://orcid.org/0000-0003-0007-6796
David J. Adams https://orcid.org/0000-0002-7030-2288
Quentin Kaas https://orcid.org/0000-0001-9988-6152

REFERENCES

Alexander, S. P. H., Peters, J. A., Kelly, E., Marrion, N. V., Faccenda, E., Harding, S. D., … CGTP Collaborators. (2017). The Concise Guide to PHARMACOLOGY 2017/18: Ligand-gated ion channels. *British Journal of Pharmacology*, *174*, S130–S159. https://doi.org/10.1111/bph.13879

Bertrand, D., Devillers-Thiéry, A., Revah, F., Galzi, J. L., Hussy, N., Mulle, C., … Changeux, J. P. (1992). Unconventional pharmacology of a neuronal nicotinic receptor mutated in the channel domain. *Proceedings of the National Academy of Sciences of the United States of America*, *89*(4), 1261–1265. https://doi.org/10.1073/pnas.89.4.1261

Bouzat, C. (2012). New insights into the structural bases of activation of Cys-loop receptors. *Journal of Physiology*, *106*(1–2), 23–33. https://doi.org/10.1016/j.jphysparis.2011.09.012

Bouzat, C., Gumilar, F., Spitzmaul, G., Wang, H.-L., Rayes, D., Hansen, S. B., … Sine, S. M. (2004). Coupling of agonist binding to channel gating in an ACh-binding protein linked to an ion channel. *Nature*, *430*(7002), 896–900. https://doi.org/10.1038/nature02753

Boyd, N. D., & Cohen, J. B. (1980). Kinetics of binding of [^{3}H]acetylcholine and [^{3}H]carbamoylcholine to Torpedo postsynaptic membranes: Slow conformational transitions of the cholinergic receptor. *Biochemistry*, *19*(23), 5344–5353. https://doi.org/10.1021/bi00564a031

Brejc, K., van Dijk, W. J., Klaassen, R. V., Schuurmans, M., van Der Oost, J., Smit, A. B., & Sixma, T. K. (2001). Crystal structure of an ACh-binding protein reveals the ligand-binding domain of nicotinic receptors. *Nature*, *411*(6835), 269–276. https://doi.org/10.1038/35077011

Calimet, N., Simoes, M., Changeux, J.-P., Karplus, M., Taly, A., & Cecchini, M. (2013). A gating mechanism of pentameric ligand-gated ion channels. *Proceedings of the National Academy of Sciences of the United States of America*, *110*(42), E3987–E3996. https://doi.org/10.1073/pnas.1313785110

Case, D. A., Cheatham, T. E. 3rd, Darden, T., Gohlke, H., Luo, R., Merz, K. M. Jr., … Woods, R. J. (2005). The Amber biomolecular simulation programs. *Journal of Computational Chemistry*, *26*(16), 1668–1688. https://doi.org/10.1002/jcc.20290

Cecchini, M., & Changeux, J.-P. (2015). The nicotinic acetylcholine receptor and its prokaryotic homologues: Structure, conformational transitions & allosteric modulation. *Neuropharmacology*, *96*, 137–149. https://doi.org/10.1016/j.neuropharm.2014.12.006

Changeux, J.-P. (2012). The nicotinic acetylcholine receptor: The founding father of the pentameric ligand-gated ion channel superfamily. *Journal of Biological Chemistry*, 287(48), 40207–40215. https://doi.org/10.1074/jbc.R112.407668

Chiodo, L., Malliavin, T. E., Giuffrida, S., Maragliano, L., & Cottone, G. (2018). Closed-locked and apo-resting state structures of the human α7 nicotinic receptor: A computational study. *Journal of Chemical Information and Modeling*, 58(11), 2278–2293. https://doi.org/10.1021/acs.jcim.8b00412

Crossthwaite, A. J., Bigot, A., Camblin, P., Goodchild, J., Lind, R. J., Slater, R., & Maienfisch, P. (2017). The invertebrate pharmacology of insecticides acting at nicotinic acetylcholine receptors. *Journal of Pesticide Science*, 42(3), 67–83. https://doi.org/10.1584/jpestics.D17-019

daCosta, C. J. B., & Baenziger, J. E. (2013). Gating of pentameric ligand-gated ion channels: Structural insights and ambiguities. *Structure*, 1(8), 1271–1283. https://doi.org/10.1016/j.str.2013.06.019

Darden, T., York, D., & Pedersen, L. (1993). Particle mesh Ewald: An N[middot] log (N) method for Ewald sums in large systems. *Journal of Chemical Physics*, 98, 10089–10092. https://doi.org/10.1063/1.464397

Dickson, C. J., Madej, B. D., Skjevik, Å. A., Betz, R. M., Teigen, K., Gould, I. R., & Walker, R. C. (2014). Lipid14: The Amber lipid force field. *Journal of Chemical Theory and Computation*, 10(2), 865–879. https://doi.org/10.1021/ct4010307

Dineley, K. T., Pandya, A. A., & Yakel, J. L. (2015). Nicotinic ACh receptors as therapeutic targets in CNS disorders. *Trends in Pharmacological Sciences*, 36(2), 96–108. https://doi.org/10.1016/j.tips.2014.12.002

Du, J., Lü, W., Wu, S., Cheng, Y., & Gouaux, E. (2015). Glycine receptor mechanism elucidated by electron cryo-microscopy. *Nature*, 526(7572), 224–229. https://doi.org/10.1038/nature14853

Grossfield, A., Pitman, M. C., Feller, S. E., Soubias, O., & Gawrisch, K. (2008). Internal hydration increases during activation of the G-protein-coupled receptor rhodopsin. *Journal of Molecular Biology*, 381(2), 478–486. https://doi.org/10.1016/j.jmb.2008.05.036

Grupe, M., Grunnet, M., Bastlund, J. F., & Jensen, A. A. (2015). Targeting α4β2 nicotinic acetylcholine receptors in central nervous system disorders: Perspectives on positive allosteric modulation as a therapeutic approach. *Basic & Clinical Pharmacology & Toxicology*, 116(3), 187–200. https://doi.org/10.1111/bcpt.12361

Gupta, S., Chakraborty, S., Vij, R., & Auerbach, A. (2017). A mechanism for acetylcholine receptor gating based on structure, coupling, phi, and flip. *Journal of General Physiology*, 149(1), 85–103. https://doi.org/10.1085/jgp.201611673

Harding, S. D., Sharman, J. L., Faccenda, E., Southan, C., Pawson, A. J., Ireland, S., … NC-IUPHAR. (2018). The IUPHAR/BPS Guide to PHARMACOLOGY in 2018: Updates and expansion to encompass the new guide to IMMUNOPHARMACOLOGY. *Nucleic Acids Research*, 46, D1091–D1106. https://doi.org/10.1093/nar/gkx1121

Hucho, F., & Changeux, J.-P. (1973). Molecular weight and quaternary structure of the cholinergic receptor protein extracted by detergents from *Electrophorus electricus* electric tissue. *FEBS Letters*, 38(1), 11–15. https://doi.org/10.1016/0014-5793(73)80500-9

Lee, J., Cheng, X., Swails, J. M., Yeom, M. S., Eastman, P. K., Lemkul, J. A., & Im, W. (2016). CHARMM-GUI input generator for NAMD, GROMACS, AMBER, OpenMM, and CHARMM/OpenMM simulations using the CHARMM36 additive force field. *Journal of Chemical Theory and Computation*, 12(1), 405–413. https://doi.org/10.1021/acs.jctc.5b00935

Liu, X., Xu, Y., Li, H., Wang, X., Jiang, H., & Barrantes, F. J. (2008). Mechanics of channel gating of the nicotinic acetylcholine receptor. *PLoS Computational Biology*, 4(1), e19. https://doi.org/10.1371/journal.pcbi.0040019

Maier, J. A., Martinez, C., Kasavajhala, K., Wickstrom, L., Hauser, K. E., & Simmerling, C. (2015). ff14SB: Improving the accuracy of protein side chain and backbone parameters from ff99SB. *Journal of Chemical Theory and Computation*, 11(8), 3696–3713. https://doi.org/10.1021/acs.jctc.5b00255

Michaud-Agrawal, N., Denning, E. J., Woolf, T. B., & Beckstein, O. (2011). MDAnalysis: A toolkit for the analysis of molecular dynamics simulations. *Journal of Computational Chemistry*, 32(10), 2319–2327. https://doi.org/10.1002/jcc.21787

Miller, P. S., & Aricescu, A. R. (2014). Crystal structure of a human GABA$_A$ receptor. *Nature*, 512(7514), 270–275. https://doi.org/10.1038/nature13293

Morales-Perez, C. L., Noviello, C. M., & Hibbs, R. E. (2016). X-ray structure of the human α4β2 nicotinic receptor. *Nature*, 538(7625), 411–415. https://doi.org/10.1038/nature19785

Nemecz, Á., Prevost, M. S., Menny, A., & Corringer, P.-J. (2016). Emerging molecular mechanisms of signal transduction in pentameric ligand-gated ion channels. *Neuron*, 90(3), 452–470. https://doi.org/10.1016/j.neuron.2016.03.032

Oswald, R. E., & Changeux, J.-P. (1982). Crosslinking of α-bungarotoxin to the acetylcholine receptor from *Torpedo marmorata* by ultraviolet light irradiation. *FEBS Letters*, 139(2), 225–229. https://doi.org/10.1016/0014-5793(82)80857-0

Plested, A. J. R. (2016). Structural mechanisms of activation and desensitization in neurotransmitter-gated ion channels. *Nature Structural & Molecular Biology*, 23(6), 494–502. https://doi.org/10.1038/nsmb.3214

Purohit, P., & Auerbach, A. (2013). Loop C and the mechanism of acetylcholine receptor-channel gating. *Journal of General Physiology*, 141(4), 467–478. https://doi.org/10.1085/jgp.201210946

Quick, M. W., & Lester, R. A. J. (2002). Desensitization of neuronal nicotinic receptors. *Journal of Neurobiology*, 53(4), 457–478. https://doi.org/10.1002/neu.10109

Revah, F., Bertrand, D., Galzi, J. L., Devillers-Thiéry, A., Mulle, C., Hussy, N., … Changeux, J. P. (1991). Mutations in the channel domain alter desensitization of a neuronal nicotinic receptor. *Nature*, 353(6347), 846–849. https://doi.org/10.1038/353846a0

Rollema, H., & Hurst, R. S. (2018). The contribution of agonist and antagonist activities of α4β2* nAChR ligands to smoking cessation efficacy: A quantitative analysis of literature data. *Psychopharmacology*, 235(9), 2479–2505. https://doi.org/10.1007/s00213-018-4921-9

Ryckaert, J.-P., Ciccotti, G., & Berendsen, H. J. (1977). Numerical integration of the cartesian equations of motion of a system with constraints: Molecular dynamics of n-alkanes. *Journal of Computational Physics*, 23(3), 327–341. https://doi.org/10.1016/0021-9991(77)90098-5

Shahsavar, A., Gajhede, M., Kastrup, J. S., & Balle, T. (2016). Structural studies of nicotinic acetylcholine receptors: Using acetylcholine-binding protein as a structural surrogate. *Basic & Clinical Pharmacology & Toxicology*, 118(6), 399–407. https://doi.org/10.1111/bcpt.12528

Shahsavar, A., Kastrup, J. S., Nielsen, E. Ø., Kristensen, J. L., Gajhede, M., & Balle, T. (2012). Crystal structure of *Lymnaea stagnalis* AChBP complexed with the potent nAChR antagonist DHβE suggests a unique mode of antagonism. *PLoS ONE*, 7(8), e40757. https://doi.org/10.1371/journal.pone.0040757

Shirts, M. R. (2013). Simple quantitative tests to validate sampling from thermodynamic ensembles. *Journal of Chemical Theory and Computation*, 9(2), 909–926. https://doi.org/10.1021/ct300688p

Smart, O. S., Neduvelil, J. G., Wang, X., Wallace, B. A., & Sansom, M. S. (1996). HOLE: A program for the analysis of the pore dimensions of ion channel structural models. *Journal of Molecular Graphics*, 14(6), 354–360, 376. https://doi.org/10.1016/S0263-7855(97)00009-X

Tabassum, N., Ma, Q., Wu, G., Jiang, T., & Yu, R. (2017). Exploring the binding energy profiles of full agonists, partial agonists, and antagonists of the α7 nicotinic acetylcholine receptor. *Journal of Molecular Modeling*, *23*(9), 251. https://doi.org/10.1007/s00894-017-3419-4

Unwin, N. (2005). Refined structure of the nicotinic acetylcholine receptor at 4Å resolution. *Journal of Molecular Biology*, *346*(4), 967–989. https://doi.org/10.1016/j.jmb.2004.12.031

Walsh, R. M., Roh, S.-H., Gharpure, A., Morales-Perez, C. L., Teng, J., & Hibbs, R. E. (2018). Structural principles of distinct assemblies of the human α4β2 nicotinic receptor. *Nature*, *557*(7704), 261–265. https://doi.org/10.1038/s41586-018-0081-7

Wang, J., Wolf, R. M., Caldwell, J. W., Kollman, P. A., & Case, D. A. (2004). Development and testing of a general amber force field. *Journal of Computational Chemistry*, *25*(9), 1157–1174. https://doi.org/10.1002/jcc.20035

Williams, C. J., Headd, J. J., Moriarty, N. W., Prisant, M. G., Videau, L. L., Deis, L. N., … Richardson, D. C. (2018). MolProbity: More and better reference data for improved all-atom structure validation. *Protein Science*, *27*(1), 293–315. https://doi.org/10.1002/pro.3330

SUPPORTING INFORMATION

Additional supporting information may be found online in the Supporting Information section at the end of the article.